ACS Catalysis

pubs.acs.org/acscatalysis

Research Article

Azide-Alkyne Click Chemistry over a Heterogeneous Copper-Based Single-Atom Catalyst

Gianvito Vilé,* Giovanni Di Liberto, Sergio Tosoni, Alessandra Sivo, Vincenzo Ruta, Maarten Nachtegaal, Adam H. Clark, Stefano Agnoli, Yajun Zou, Aleksandr Savateev, Markus Antonietti, and Gianfranco Pacchioni

Cite This: *ACS Catal.* 2022, 12, 2947−2958

Read Online

ACCESS | Metrics & More | Article Recommendations | Supporting Information

ABSTRACT: One-pot three-component regioselective azide-alkyne cycloadditions are central reactions for synthesizing pharmaceuticals and fine chemicals and are also applied for *in vivo* metabolic labeling biotechnology. Homogeneous catalysts based on copper species coordinated with ancillary ligands are regularly used to perform this reaction, offering superior catalytic activity and selectivity compared to conventional heterogeneous counterparts based on supported copper nanoparticles. However, the challenge of catalyst recovery limits the use of these homogeneous compounds in many large-scale applications. In this work, we report the high catalytic performance of a family of Cu-based single-atom catalysts for triazole synthesis, with an emphasis on the fundamental understanding of the structure and function of the catalyst. The catalysts were prepared via tricyanomethanide polymerization to create a joint electronic structure where the mesoporous graphitic carbon nitride carrier acts as a ligand for the atomically dispersed copper species. The material properties and the precise metal location/coordination (i.e., deposited in the heptazine pore of carbon nitride, substituted in the framework of carbon nitride, hosted in a vacancy, or entrapped in sandwich-like arrangement) were characterized through a battery of spectroscopic and theoretical methods. The catalysts were employed in the synthesis of 1,2,3-triazoles employing azide-alkyne click reaction under base-free conditions. The single-atom Cu catalysts demonstrated improved activity and selectivity compared to the homogeneous reference catalyst. Density functional theory calculations corroborated the results and showed that the reaction proceeds through a barrier given by the activation of the acetylenic moiety on Cu_1. The activity of this step was primarily affected by the coordination of the metal with the support. Therefore, understanding the metal coordination in single-atom catalysts is critical to further optimizing single-atom catalysts and greening synthetic chemistry.

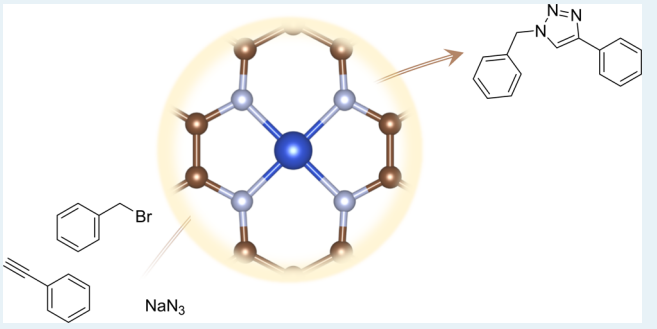

KEYWORDS: *single-atom catalysis, sustainable chemistry, azide-alkyne cycloadditions, triazole synthesis, heterogeneous catalysis*

1. INTRODUCTION

Synthetic methodologies that exploit metal-based homogeneous catalysts are of paramount importance for the fast and high-throughput production of chemicals. The azide-alkyne click cycloaddition is an example of such important homogeneous reactions generating triazoles,[1,2] key motifs for the preparation of drugs, pesticides, natural compounds, and functional materials.[3,4] The synthesis can proceed via a three-component reaction involving aryl bromide, sodium azide, and alkyne, or via the two-component reaction involving aryl azide and alkyne. However, organic azides are not often commercially available (particularly when dealing with highly-substituted intermediates) and have an explosive character.[5] Hence, three-component reaction is the preferred choice for the synthesis of triazoles in industrial settings, due to the facile scale-up, the possibility to rely on cheaper and readily available starting materials, and the advantage of not having to stock a large amount of organic azides.[5]

The three-component reactions prototypically occur in the presence of homogeneous catalysts based on copper. Over the last two decades, catalytic systems featuring the use of a wide variety of ancillary ligands, including phosphines, N-heterocyclic carbenes, bipyridines, and acyclic diaminocarbenes, have been successfully reported.[6−11] Due to their uniform and well-defined active sites, these homogeneous catalysts show remarkable

Received: December 6, 2021
Revised: February 2, 2022
Published: February 17, 2022

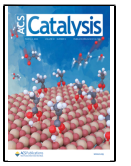

selectivity and a high turnover frequency. However, they also suffer from practical issues such as rapid catalyst deactivation and product contamination with metal residues, that challenge the recovery and reuse of the homogeneous catalyst.[12] To overcome these issues, the design and exploitation of heterogeneous catalysts with immobilized copper species is an attractive direction for research and development. These materials are widely preferred since they are stable and easy to separate from the reaction mixture. Various heterogeneous catalysts have been fabricated for the azide-alkyne click cycloaddition reaction using bare or ligand-modified copper on silica, carbon-based materials, zeolites, and polymeric materials.[13−16] However, these systems suffer from several other drawbacks, including the presence of heterogeneous active sites on solid surfaces.[17,18] This complicates the description of the reactivity of the azide-alkyne cycloaddition catalyst featuring supported copper nanoparticles[19,20] since the nanoparticle contains a variety of atoms with different coordinations (*i.e.*, atoms at the vertices, edges, facets) and defects (*i.e.*, steps, kinks, vacancies). This intrinsic complexity poses a significant challenge in understanding the "active center" and establishing structure−activity relationships.[17] Even with the impressive number of physicochemical tools in surface science,[21] the level of understanding of nanoparticle-based copper catalysts for triazole synthesis is limited and the design process remains empirical. Moreover, due to the weak interactions between the support and the copper species, some of these heterogeneous copper catalysts suffer from fatal shortcomings such as loss of the active sites and reduced selectivity. Recent studies have revealed that the performance of these heterogeneous catalysts relies on the rational design of the copper ensemble size.[14,15] Hence, it appears to be key to tailor the synthesis of the heterogeneous copper catalysts to reach good catalytic efficiency, excellent selectivity, high stability, and good recyclability.

Single-atom catalysts (SACs) with atomically dispersed metals entrapped in the cavities of inert carriers are emerging as a new class of nanocatalysts[22] and are gaining considerable attention because of the possibility to reach 100% metal atom utilization with excellent catalytic behavior compared with traditionally supported nanoparticles.[23−33] A strong metal−support interaction is thought to be critical to prevent aggregation of single atoms on the surface.[34−41] However, the relation between the exact metal coordination and the catalytic performance is often not elaborated. Bearing in mind the importance of triazoles and given recent reports showing the manufacturing of triazoles over single-atom catalytic systems,[42] we report the development of a copper-based SAC supported on a mesoporous polymeric graphitic carbon nitride motif. The SAC catalyst was extensively characterized by experimental and theoretical methods to unlock structure−property relationships and understand the reactivity of the materials. These findings may pave a new path toward heterogenization of homogeneous copper catalysts for other cycloaddition reactions.

2. MATERIALS AND METHODS

2.1. Catalyst Preparation. All reagents (sodium tricyanomethanide (98%), $CuCl_2{\cdot}2H_2O$ (≥99%), cyanamide (99%), a 40% aqueous dispersion of 12 nm SiO_2 particles, and NH_4HF_2 (95%)) were purchased (IoLiTec, Sigma-Aldrich) and used as such, without any further purification. To prepare copper(II) tricyanomethanide, a solution of $CuCl_2{\cdot}2H_2O$ (1.70 g, 0.01 mol) in water (10 mL) was added to a stirred solution of sodium tricyanomethanide (1.13 g, 0.01 mol) in water (10 mL). The obtained mixture was stirred in the dark for 3 h. A brown solid was separated by centrifugation at 4000 rpm, washed with water (three times with 10 mL each), and dried in vacuum (7 mbar, 50 °C) to obtain 0.95 g of material.

The synthesis of two Cu-based single-atom catalysts (herein indicated as saCu-*x*@mpgC_3N_4, where *x* designates the different materials), was performed by mixing cyanamide (3.0 g), copper(II) tricyanomethanide, and Ludox HS40 (7.5 g) and stirring the obtained solution at 70 °C for 16 h, until the water was completely evaporated. For saCu-1@mpgC_3N_4 and saCu-2@mpgC_3N_4, 37 mg (0.15 mmol) and 131 mg (0.53 mmol) of copper(II) tricyanomethanide were used, respectively. The resulting solid was calcined at 550 °C for 4 h, using a heating rate of 550 °C. The resulting brown-yellow powder was ground and treated with an NH_4HF_2 solution (12 g in 50 mL of water) for 24 h to remove the silica template. The suspension was centrifuged, and the precipitate was washed three times with distilled water and once with ethanol. Finally, the product was dried at 60 °C under vacuum overnight, obtaining 1.78 and 1.61 g of saCu-1@mpgC_3N_4 and saCu-2@mpgC_3N_4, respectively. The procedure for preparing mpgC_3N_4 was similar to that of saCu-*x*@mpgC_3N_4 except that no metal tricyanomethanide was added.

2.2. Catalyst Characterization. Powder X-ray diffraction (XRD) patterns were collected on a Bruker D8 Advance diffractometer equipped with a scintillation counter detector and with Cu Kα radiation (λ = 0.15418 nm) using a 0.01° s^{-1} (2θ) scanning speed. Carbon, hydrogen, nitrogen, and sulfur elemental analysis was accomplished by combustion analysis using a Vario Micro device. Inductively coupled plasma optical emission spectroscopy (ICP-OES) was performed using an Optima 8000 ICP-OES spectrometer (PerkinElmer) to determine the copper content. Nitrogen physisorption was performed on a Micromeritics ASAP 3020 instrument (Micromeritics, Atlanta) at −196 °C. Before the measurement, the samples (*ca.* 20−40 mesh) were degassed at 150 °C for 24 h. The specific surface area was determined by the Brunauer−Emmett−Teller (BET) method using the adsorption branch in the p/p_0 range of 0.05−0.35. The micropore and mesopore volumes were calculated using the quenched solid density functional theory (QSDFT) model for N_2 adsorbed on carbon with a cylindrical pore shape at 77 K. Scanning electron microscopy (SEM) and energy-dispersive X-ray (EDX) images were obtained on a JSM-7500F (JEOL) at an accelerating voltage of 3 kV. EDX investigations were conducted using a Link ISIS-300 system (Oxford Microanalysis Group) equipped with a Si(Li) detector and an energy resolution of 133 eV. Transmission electron microscopy (TEM) studies were performed using a double Cs-corrected JEOL JEM-ARM200F (S)TEM operated at 80 kV equipped with a cold field emission gun. X-ray photoelectron spectroscopy (XPS) measurements were carried out in a custom-designed UHV system working at the base pressure of 1×10^{-9} mbar and equipped with an electron analyzer (EA125 Omicron) and an X-ray source (DAR400 Omicron). The powder samples were suspended in methanol and drop-cast on metal support to obtain a homogeneous film. Once dried, the sample was introduced in an ultrahigh-vacuum system and left outgassing overnight. Photoemission spectra were acquired at room temperature in normal emission. The spectra were analyzed using the XPSPEAK software using Voigt functions and subtracting a Shirley background. X-ray absorption spectroscopy (XAS) experiments were performed at the SuperXAS beamline of the Swiss Light Source at the Paul Scherrer Institute in Villigen, Switzerland. The Swiss Light

https://doi.org/10.1021/acscatal.1c05610
ACS Catal. 2022, 12, 2947−2958

Table 1. Compositional and Textural Properties of Heterogeneous Catalysts

catalyst	C/wt %	N/wt %	H/wt %	C/N ratio/-	C/H ratio/-	Cu/wt %	S_{BET}/m^2 g^{-1}	V_{pore}/cm^3 g^{-1}
mpgC_3N_4	31.90	48.75	2.43	0.66	13.16	0.0	157	0.46
saCu-1@mpgC_3N_4	31.58	49.05	2.47	0.64	12.80	0.5	264	0.68
saCu-2@mpgC_3N_4	31.74	48.90	2.47	0.65	12.98	1.6	257	0.71

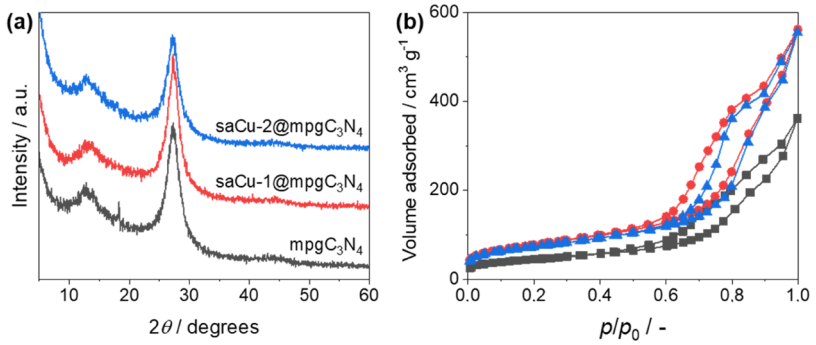

Figure 1. X-ray diffraction patterns (a) and N_2-physisorption isotherms (b) of heterogeneous catalysts. Color codes in (a) apply to both sections.

Source operates in top-up mode at 400 mA and 2.4 GeV. Radiation from a 2.9 T bending magnet was collimated using a Si-coated collimating mirror at 2.9 mrad (which also served to reject higher harmonics) channel-cut monochromator. Focusing of the beam to a spot size of 1.0 mm × 0.2 mm on the sample was achieved by a Rh-coated toroidal mirror. The beamline provides an X-ray flux of 6×10^{11} photon s^{-1} and an energy bandwidth of 1 eV at the Cu K-edge. XAS spectra of samples pressed to pellets were collected in transmission mode using a 20 cm long ionization chamber filled with 1 bar nitrogen. Spectra were collected with a 1 Hz scanning speed (quick-scanning mode), and 300 spectra were averaged per sample. The data were processed using ProQEXAFS[43] to calibrate, normalize, and average the obtained XAS spectra with subsequent EXAFS analysis performed within the Demeter software package.[44] The fitting of the EXAFS was conducted using theoretical structures for Cu placed within the hollows of the mpgC_3N_4 structure representing d4-planar and octahedral symmetry.

2.3. Catalyst Performance. For reactions catalyzed by heterogeneous catalysts, the alkyne (0.5 mmol), sodium azide (0.5 mmol), and alkyl halide (0.5 mmol) were dissolved in a glass tube in 5 mL of solvent dimethylformamide (DMF), and the catalyst (30 mg) was added. The tube was sealed and heated in an oil bath at 100−140 °C for 0−30 min. After completion of the reaction, the catalyst was filtered; washed with ethyl acetate, water, and ethanol; dried at 60 °C for 6 h; and reused in a subsequent reaction run. For reactions catalyzed by homogeneous catalysts, the alkyne (0.5 mmol), sodium azide (0.5 mmol), and alkyl halide (0.5 mmol) were dissolved in 5 mL of solvent (DMF) and the catalyst (1 equiv of Cu, to have comparable Cu amounts as in saCu-2@mpgC_3N_4) was added. $CuCl_2$ (Sigma-Aldrich, 99.995% trace metals basis), CuCl (Sigma-Aldrich, ≥99.995% trace metals basis), CuI (Sigma-Aldrich, ≥99.5%), and $[Cu(COD)Cl]_2$ (Sigma-Aldrich, 95%) were used as catalysts. The reaction tube was sealed and heated in an oil bath at 100−140 °C for 0−30 min. In all cases, the crude products were extracted by washing with ethyl acetate and analyzed by ^{1}H NMR and ^{13}C NMR spectra on a Bruker 400 MHz spectrometer ($CDCl_3$).

2.4. Theoretical Calculations. Density functional theory (DFT) calculations were performed with the VASP code.[45,46] H(1s), C(2s, 2p), N(2s, 2p), Na(2s, 2p, 3s), and Cu(3d, 4s) electrons were treated explicitly, and the interaction between the inner electrons and the nuclei was treated with the projector augmented wave method.[47,48] The exchange-correlation functional proposed by Perdew, Burke, and Ernzerhof (PBE) was adopted.[49] The long-range dispersion was added to the potential according to Grimme's DFT + D3 scheme with a Becke−Johnson damping function.[50,51] Structure relaxations were performed at the Γ point with a cutoff of 400 eV. Spin-polarization effects were included in all calculations. Dipole and quadrupole corrections to the total energy were applied along the nonperiodic direction for all calculations on slab models. A vacuum region of at least 1.5 nm was included along the nonperiodic direction in the supercell to avoid spurious interactions between a replica of the slab models. As widely discussed in the literature, carbon nitride nanosheets have been modeled assuming a corrugated heptazine structure.[52−54]

Gibbs free energies profiles have been determined by adopting the computational approach pioneered by Nørskov and co-workers,[55,56] to study reactions involving gas-phase molecules,[57−60] where we added the standard entropies of gas species to the calculated DFT energies. The entropy of acetylene (200.9 J mol^{-1} K^{-1}) has been taken from the literature.[61,62]

3. RESULTS AND DISCUSSION

3.1. Structural, Textural, and Compositional Properties of Fresh Materials. The two Cu-based single-atom catalysts have been prepared by polymerization of copper tricyanomethanide salts with cyanamide in the presence of a SiO_2 template. Removal of the template by treatment with $(NH_4)HF_2$ gives the ordered mesoporous structure of the material, increasing the specific surface area of bare gC_3N_4, which is generally around 5−10 to >150 m^2 g^{-1} (Table 1).[63] The final composition of the reference carbon nitride and single-atom samples is shown in Table 1. In particular, all materials are characterized by a stoichiometric C/N ratio of *ca.* 0.65, in line with the literature for mesoporous graphitic C_3N_4, and the loading of Cu is 0.5 wt % over saCu-1@mpgC_3N_4 and 1.6 wt % over saCu-2@mpgC_3N_4.

Structurally, catalysts are like the reference mesoporous graphitic carbon nitride, as shown by X-ray diffraction patterns (Figure 1a). The samples have two characteristic (and broad) diffraction peaks at 13 and 27°, which are assigned to the in-

https://doi.org/10.1021/acscatal.1c05610
ACS Catal. 2022, 12, 2947−2958

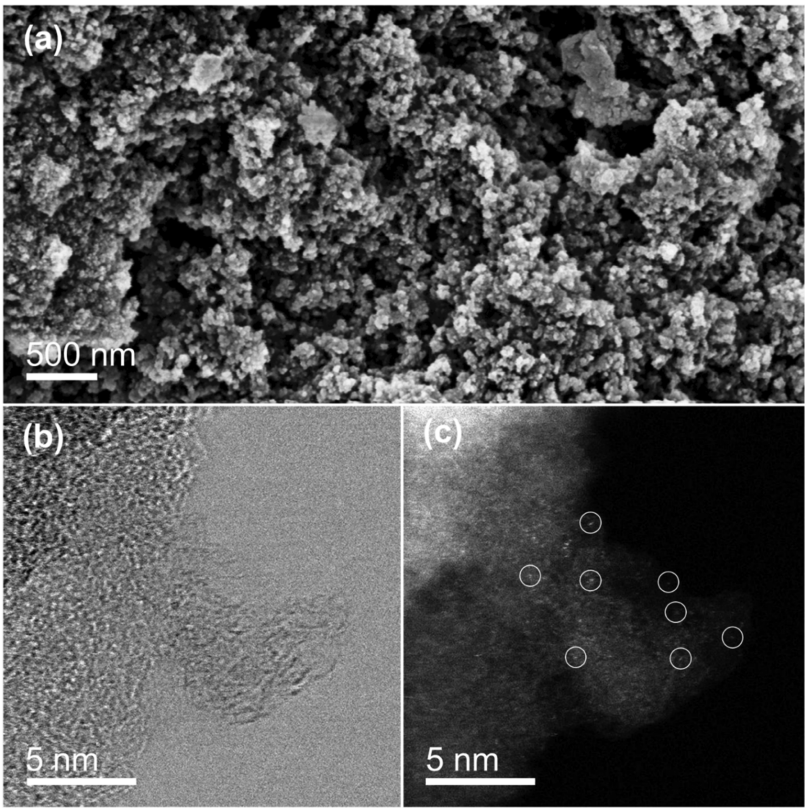

Figure 2. Scanning electron micrographs (a), high-resolution transmission electron microscopy (b), and aberration-corrected high-angle annular dark-field transmission electron microscopy of saCu-2@mpgC_3N_4 (c).

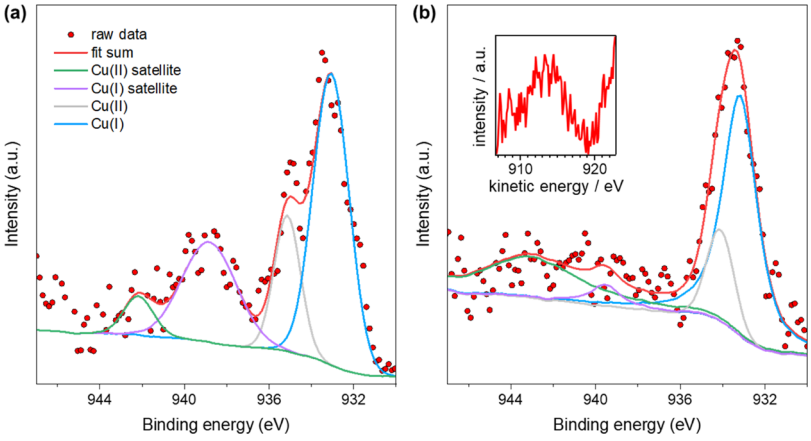

Figure 3. Cu 2p X-ray photoelectron spectra of saCu-1@mpgC_3N_4 (a) and saCu-2@mpgC_3N_4 (b). The inset in (b) refers to the high-resolution analysis of the Auger peak in the same catalyst.

plane structural packing motif and to the interplanar stacking of aromatic systems identified as the (002) peak, respectively.[63] The presence of copper in the framework is accompanied by a slight disturbance of the local C_3N_4 network. This is illustrated by the intensity decrease and broadening of the stacking reflection at the $2\theta = 27°$ XRD peak in Figure 1a, suggesting the increased distortion of the stacking arrangement of the carbon nitride layers and the decrease of the crystallite size in the resulting products upon the increase of the amount of copper.

N_2 physisorption analysis indicates that the materials have type IV isotherms with H3 hysteresis loops indicating mesoporous structure in the synthesized materials (Figure 1b, see also Figure S1 in the Supporting Information). The S_{BET} surface areas are 264 and 257 $m^2\ g^{-1}$ for saCu-1@mpgC_3N_4 and saCu-2@mpgC_3N_4, respectively. The morphology of the catalysts is in both cases made of particles with no specific shape and a diameter of *ca.* 20−200 nm (Figure 2). The TEM micrograph of a representative catalyst shows the presence of characteristic mesopores of 5−20 nm, which originate from the removal of the template (Figure 2). High-angle annular dark-field scanning transmission electron microscopy (HAADF-STEM) investigation performed on an aberration-corrected microscope showed that copper is uniformly distributed across the mpgC_3N_4 support and is in an atomically dispersed form (Figure 2). No regions of pronounced local intensity are seen in the Cu map, in line with the absence of nanoparticles.

https://doi.org/10.1021/acscatal.1c05610
ACS Catal. 2022, 12, 2947−2958

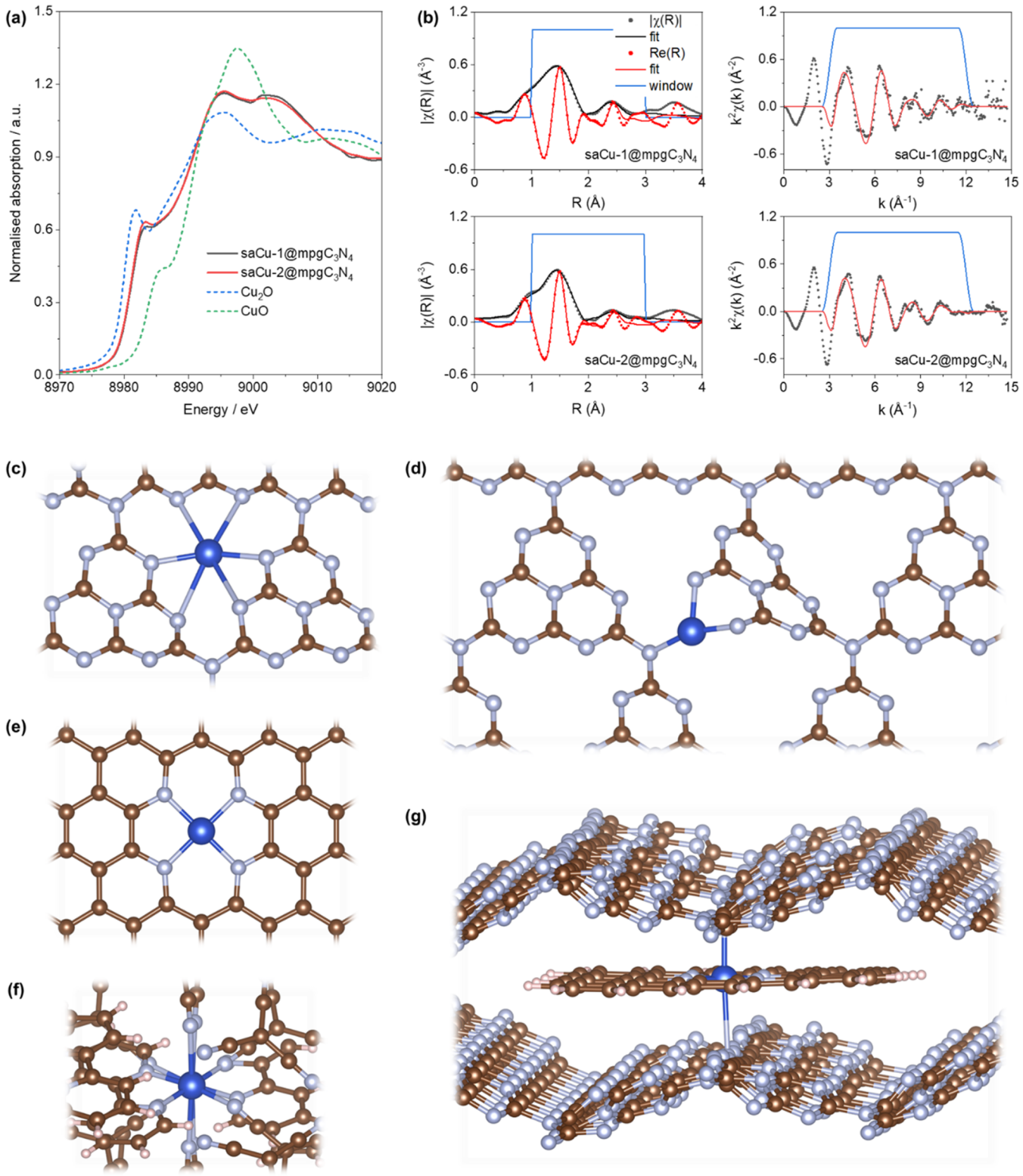

Figure 4. (a) Copper K-edge X-ray absorption near-edge structure of the two single-atom catalysts and of reference CuO and Cu_2O. (b) Extended X-ray absorption fine structure of saCu-1@$mpgC_3N_4$ (top) and saCu-2@$mpgC_3N_4$ (bottom). (c−g) Possible model structures of Cu-based single-atom catalysts. The structural feature Cu adsorbed in the heptazinic pore of $mpgC_3N_4$ (c), Cu substituting C in $mpgC_3N_4$ (d), Cu hosted in a dicarbon vacancy in N-doped graphene (e), octahedral complex $[Cu(bpy)(tcm)_4]^{2+}$ (f), and sandwich-like arrangement of Cu-doped N-graphene intercalated in $mpgC_3N_4$ (g).

3.2. Understanding Single-Atom Metal Coordination and Charge Transfer. X-ray photoelectron spectroscopy was applied to determine the surface chemistry of the materials. Regarding the support (Figures S2 and S3 in the Supporting Information), the C 1s photoemission spectrum indicates a complex structural situation: a strong peak centered at 288.3 eV suggests the presence of carbon bonded to three nitrogen atoms, which is the fingerprint of $mpgC_3N_4$,[64] whereas the two other

https://doi.org/10.1021/acscatal.1c05610
ACS Catal. 2022, 12, 2947−2958

Table 2. Structural Information Derived from EXAFS Analysis of the Single-Atom Catalysts

catalyst	coordination sphere	scattering path	NN[a]	σ^{2b}	R[c]
saCu-1@mpgC_3N_4	1st	Cu−C/N/O	5.2 ± 0.5	0.010 ± 0.002	1.92 ± 0.02
	2nd	Cu−C/N/O	4.0 ± 0.4	0.008 ± 0.002	2.88 ± 0.03
saCu-2@mpgC_3N_4	1st	Cu−C/N/O	4.7 ± 0.5	0.010 ± 0.002	1.92 ± 0.02
	2nd	Cu−C/N/O	4.0 ± 0.4	0.012 ± 0.003	2.89 ± 0.03

[a]Number of nearest neighbors. [b]Interatomic distance. [c]Pseudo-Debye−Waller factor.

intense peaks at 285.8 and 284.8 eV are related to C sp^3 and C sp^2 or adventitious carbon, respectively. Minor components can also be ascribed to carboxyl groups (289.5 eV) and carbide or defective carbon species (283.7 eV). The N 1s photoemission spectrum can be fitted by five main peaks: the strongest component is located at 398.4 eV and can be associated with bridging nitrogen in the triazine rings (C═N-C); the peak at 399.5 eV can be ascribed to primary amines C−NH_2; the peak at 400.8 eV is ascribed to C_2−N−H species; and the peak at 401.3 eV is ascribed to N-C_3.[65] Finally, the low-intensity feature at 396.8 eV is related to nitrides.

Surface characterization *via* X-ray photoelectron spectroscopy confirms the presence of Cu(I) ions at the surface, together with the presence of a minority Cu(II) component. As shown in Figure 3, the Cu 2p photoemission peak shows a main component at about 933.1 eV and a second less intense feature at 934.5 eV; the former can be associated with Cu(I) and the latter to Cu(II), as also confirmed by the relatively high intensity of the satellite features between 939 and 945 eV, which are typically associated with final state effects in copper species with a $3d^9$ electronic configuration.[66] The presence of a majority of Cu(I) species is also confirmed by the analysis of the Auger peak, which is centered at a kinetic energy of 914 eV, and overall, according to a Wagner plot, the electronic fingerprint observed is similar to CuC_3N_4.[67]

The fine details of copper at the atomic level were investigated by synchrotron X-ray absorption spectroscopy (XAS). As shown in Figure 4a, the absorption edge of Cu for both saCu-1@mpgC_3N_4 and saCu-2@mpgC_3N_4 is located between that of Cu_2O and CuO, suggesting the majority of the Cu atoms to be Cu (I). Furthermore, the peak at around 8981 eV, which is characteristic of the 1s−4p transition, is assigned to Cu(I).[68,69] From the fitting of the Fourier transform of the extended X-ray absorption fine structure (EXAFS) spectra (Figure 4b), it is found that Cu is surrounded by approximately five neighboring ligands at an average distance of around 1.92 Å. These results suggest that Cu atoms are in the center of the hollow structure of the support and with other four neighbors in the second coordination sphere at the distance of around 2.88 Å (Table 2). The Cu is noted as being dispersed as single atoms across the C_3N_4 support with no evidence of any scattering contribution from Cu−Cu pairs in the obtained EXAFS.

The information from the EXAFS measurements has been cross-checked by DFT calculations on C_3N_4 structures hosting Cu species on different sites. We start the discussion from a system where Cu is coordinated in a pore created by the heptazine units (Figure 4c), a commonly hypothesized adsorption site for single metal atoms.[70] Here, the Cu atom is surrounded by six N neighbors, but the N−Cu distances are larger than that observed in EXAFS and span in the range 2.1−2.7 Å (average 2.45 Å).

An alternative to the coordination of Cu_1 species in pores is represented by substitutional doping. As previously proposed in the literature,[67] Cu occupies here a C-site connecting two heptazine pores (Figure 4d). In this structure, Cu is bound to three N atoms at 1.8−1.9 Å and has four C atoms in a second coordination sphere at about 2.6−2.8 Å. Since neither simple coordination of Cu nor Cu implanted in a substitutional site entirely agrees with the XAS data, we extended the modeling to the structure reported in Figure 4e, where Cu is coordinated in a dicarbon vacancy in nitrogen-doped graphene (NG). This implies a structure of a support to be different from carbon nitride, but this choice can be rationalized if one looks at the octahedral $[Cu(bpy)(tcm)_4]^{2+}$ complex in Figure 4f. Unlike copper(II) tricyanomethanide,[71] which we used as a precursor for synthesizing single-atom catalysts based on carbon nitride motifs via copolymerization strategy and which possesses a polymeric structure, this molecular complex serves as a convenient model to reduce computational costs. Nevertheless, the copper atom in $[Cu(bpy)(tcm)_4]^{2+}$ and in copper(II) tricyanomethanide is in an octahedral environment. Another structural motif that comprises the Cu atom hosted in a dicarbon vacancy surrounded by pyridinic N-species has square-planar coordination, which closely resembles that of a copper atom bound to a bis-pyridine ligand in the $[Cu(bpy)(tcm)_4]^{2+}$ model. We, therefore, included the Cu/NG structure (Figure 4e), assuming that part of the Cu hosted in the carbon nitride matrix may be surrounded by fragments of nitrogen-doped graphene moieties also formed during synthesis. In this case, the structure relaxation yielded 1.9 Å for Cu−N and 2.7 Å for Cu−C bonds, which are in good agreement with XAS in terms of bond distances but not in terms of coordination number (four in the calculated model, five according to the experimental EXAFS). The possibility to increase the coordination number of Cu from 4 to 6 was explored by sandwiching a N-doped graphene cluster between two layers of corrugated C_3N_4 (Figure 4g): in this case, however, the coordination of the Cu to the N atoms from the C_3N_4 layers is very loose, leading to Cu−N axial distances as large as 2.9 Å, which is not in agreement with our XAS data.

It is worth noting that, despite the remarkable differences in bonding and coordination environment, all of these Cu_1 species exhibit a Cu^+ charge state, as evidenced by the projected density of states (Figure S7). Charge transfer occurs in all models since the electron donated by the metal is transferred to the conduction band of the support, and no localization is observed.

It is clear that the complete and undisputed determination of the location and coordination of single metal atoms on a support such as C_3N_4 is more complex than it could appear. However, we will use the results of structural motifs modeling shown in Figure 4c−e in the section related to calculating the reaction free-energy profile (*vide infra*). Therefore, we decided to characterize the catalytic activity of Cu species toward the synthesis of triazoles in three cases: Cu adsorbed in the heptazinic pore of C_3N_4 (Cu(ads)/C_3N_4, Figure 4c), Cu substitutional to C in C_3N_4 (Cu(sub)/C_3N_4, Figure 4d), and Cu adsorbed in the dicarbon vacancy in N-doped graphene (Cu(ads)/NG, Figure 4e). This choice is based on the fact that all of the structures mentioned above are compatible with the XAS evidence,

https://doi.org/10.1021/acscatal.1c05610
ACS Catal. 2022, 12, 2947−2958

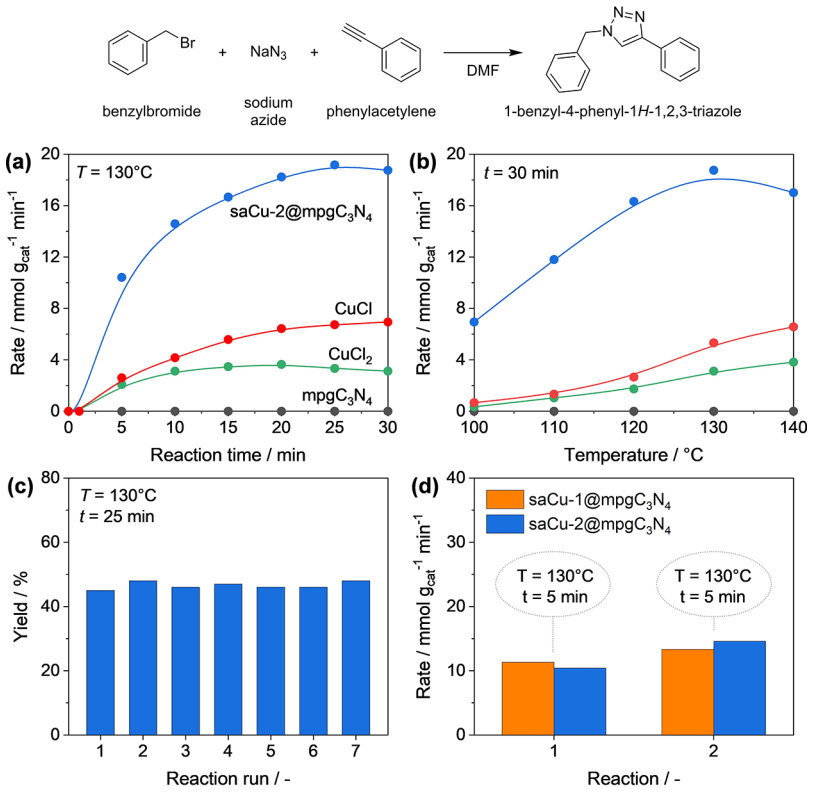

Figure 5. Synthesis of 1-benzyl-4-phenyl-1*H*-1,2,3-triazole *via* click cycloaddition between phenylacetylene, benzyl bromide, and sodium azide. The illustration shows the influence of reaction time (a) and temperature (b) on the performance of $mpgC_3N_4$, $CuCl_2$, CuCl, and saCu-2@$mpgC_3N_4$. Performance of saCu-2@$mpgC_3N_4$ over seven consecutive reaction runs under fixed conditions (c), proving the catalyst stability. Comparison between the activity of saCu-1@$mpgC_3N_4$ and saCu-2@$mpgC_3N_4$ at two different conditions (d). Color codes in (a) apply to (b)−(d) as well.

pointing to the fact that single-atom catalysts are likely made of a mixture of different kinds of sites for metal species. Therefore, the information provided via spectroscopy is often a mediated property. By computing for the first time the reaction energy profiles over different catalytic sites, we have been able to compare structural and reactivity effects over a six-coordinated Cu atom with long and loose bonds to saturated atoms of the substrate (Cu(ads)/C_3N_4), with Cu species featuring three (Cu(sub)/C_3N_4) or four short Cu−N bonds (Cu(ads)/NG).

3.3. Catalytic Performance and Molecular Understanding. Before any activity evaluation, a blank test was performed without any catalyst. Figure S4 in the Supporting Information shows that the triazole product was not formed over 30 min. This observation excludes the potential contribution of gas or liquid-phase chemistry to drive the reaction. Similarly, we have also conducted the reaction on the bare carbon nitride carrier, which did not give any product (Figure 5a,b). These results unambiguously indicate that the reaction requires copper catalysts to proceed.

The single-atom saCu-2@$mpgC_3N_4$ catalyst was evaluated in the synthesis of 1-benzyl-4-phenyl-1*H*-1,2,3-triazole *vis-a-vis* with two model homogeneous catalysts. Figure 5a shows the reaction time versus performance of the heterogeneous and homogeneous catalysts, further demonstrating the better reactivity of the heterogeneous sample. Given that the reaction was conducted using an equivalent amount of Cu in the sample, this corroborates that the ligand−metal charge transfer in the saCu-2@$mpgC_3N_4$ catalyst leads to enhanced catalytic performance. By increasing the temperature from 100 to 140 °C (Figure 5b), the reaction rate increases with both catalysts, although saCu-2@$mpgC_3N_4$ remains more active. It must be considered that all copper species in the homogeneous copper chloride catalyst are available for the reaction. On the other hand, during synthesis, some of the copper species are entrapped in the bulk of the material, and thus are inaccessible given that catalysis is a surface phenomenon. Based on this consideration, it is reasonable to assume that the discrepancy between the turnover numbers over the single-atom catalyst and homogeneous sample is even higher. The durability of the SAC material was also investigated by employing the catalyst in several consecutive reactions (Figure 5c).

After the first cycle, the material was filtered, dried, and reused in a subsequent reaction. It is noteworthy to mention that no distinct difference in the product yield was observed, and the catalytic system worked exceptionally well, even up to seven runs. ICP-MS analysis of the reaction mixture solution after the seven runs confirmed the absence of any leached Cu species in the sample. In addition, characterization of the used material by XRD and N_2 physisorption (Figure S5) proved no structural modifications, in addition to the absence of metal leaching. XPS analysis of the same catalyst (Figure S6) shows that the speciations of Cu and N after catalysis are the same, despite the small variations in the carbon spectrum that are probably due to the presence of various organic compounds adsorbed on the sample. Concerning the surface amount of Cu, this appears to be 6.2%, slightly above the value in the fresh material (4.8%) but within the instrumental error (2−3%).

Finally, Figure 5d shows the effect of metal loading in two single-atom catalysts on their performance in the studied reaction. Thus, the triazole yield was slightly higher over the saCu-2@$mpgC_3N_4$ sample. To expand the applicability of this procedure, several alkynes and azides with different function-

https://doi.org/10.1021/acscatal.1c05610
ACS Catal. 2022, 12, 2947−2958

Scheme 1. Substrate Scope for Synthesizing Substituted 1,2,3-Triazoles *via* Click Cycloaddition between Aryl Acetylenes, Benzyl Bromide, and Sodium Azide[a]

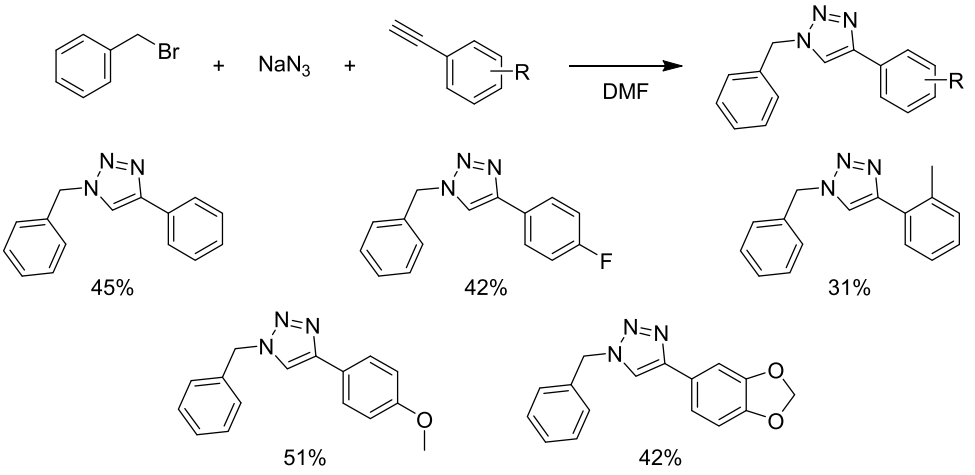

[a]Reaction conditions: Temperature, 130 °C; reaction time, 30 min; catalyst, saCu-2@mpgC_3N_4.

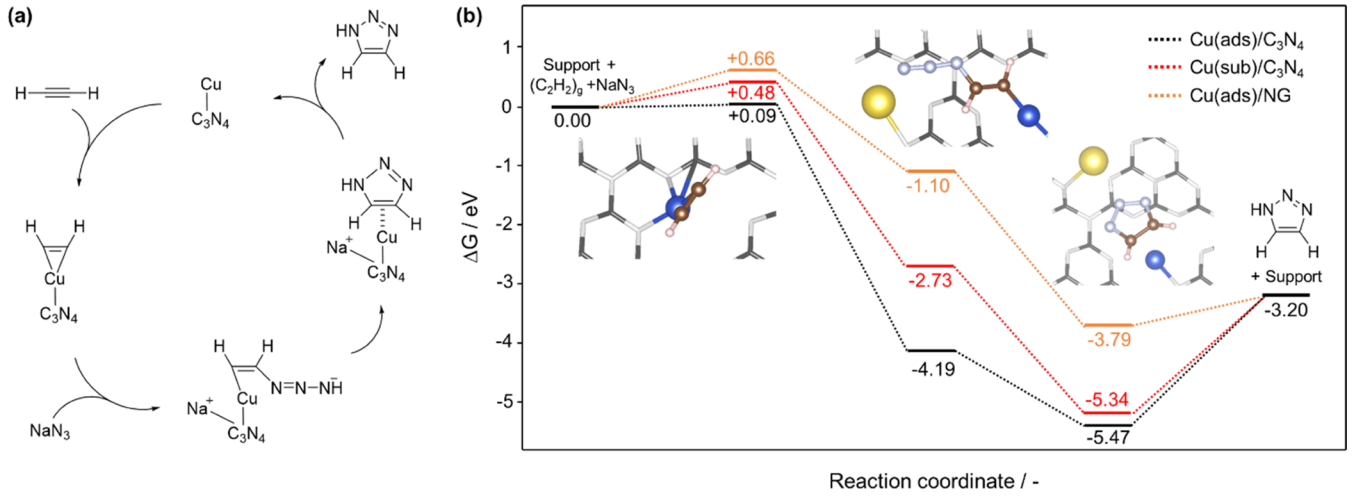

Figure 6. Proposed catalytic cycle for triazole formation over supported Cu_1 species (a). Reaction free-energy profile (b) at a temperature of 130 °C. The structures in the inset in (b) refer to the intermediates formed over Cu(ads)/C_3N_4.

alities were examined (Scheme 1). The reaction works well with various aryl halides and alkynes, tolerating electron-donating and -withdrawing functional groups in the starting material. We also conducted an additional experiment, scaling up the reaction between phenylacetylene, benzyl bromide, and sodium azide, to produce 1 g of 1-benzyl-4-phenyl-1*H*-1,2,3-triazole at 130 °C and with 30 min reaction time. The reaction proceeded well with a 40−50% yield. It is important to highlight that these investigations were conducted at a lower reaction time (25 min), and thus at a milder degree of conversion, to better appreciate catalytic differences among the materials. In Table S1, we report the corresponding turnover frequency (TOF) of our catalyst, as well as the estimated TOF of state-of-the-art Cu(I) and Cu(II) catalysts for the three-component triazole synthesis. The table highlights that our single-atom sample stands out as the most active catalyst for this reaction. This verifies that the product yield is not the most appropriate way to compare the catalytic activity of homogeneous and single-atom catalysts, and TOFs should be calculated and reported, as they account for the intrinsic reaction rate. It must be remarked that, in terms of TOFs, our catalyst is also more active than the single-atom catalyst recently reported by Yang and co-workers[42] (Table S1). Finally, we have conducted catalytic tests over other homogeneous catalysts (CuI and [Cu(COD)Cl_2], both with Cu(I) active sites; see Figure S4). The results confirm that these homogeneous catalysts are also less reactive than saCu-2@mpgC_3N_4.

DFT calculations were carried out to derive technical insights into the reaction mechanism. To this end, we studied a simplified model reaction between sodium azide and the simplest alkyne, acetylene, as shown in the reaction scheme in Figure 6a. As a first approximation, this simplification omits the steric and inductive effect of the phenyl group on the reactivity of the C−C triple bond, which is not a critical factor in identifying the reaction mechanism. The envisaged mechanism starts with the adsorption and activation of acetylene over Cu_1/C_3N_4. Then, a linear intermediate is formed upon the addition of sodium azide, with contextual loss of a Na^+ cation that binds to the carbonaceous support. Next, the cyclization completes, forming a triazolate pentacyclic ion bound to the Cu SAC. Finally, the desorption of a sodium triazolate molecule regenerates the catalyst. To verify the correctness of this mechanism, we have confirmed the preferential adsorption of the alkyne moiety over a copper single-atom catalyst by running

https://doi.org/10.1021/acscatal.1c05610
ACS Catal. 2022, 12, 2947−2958

catalytic experiments on a catalyst pretreated with one of the reagents. In particular, saCu-2@mpgC_3N_4 was first contacted with a 5 mL DMF solution of sodium azide (0.5 mmol) at 130 °C for 30 min. The catalyst was then filtered and contacted with a 5 mL DMF solution of alkyne (0.5 mmol) and alkyl halide (0.5 mmol). The reaction tube was sealed and heated at 130 °C for 30 min, but no product was formed. Then, saCu-2@mpgC_3N_4 was contacted with a 5 mL DMF solution of alkyne (0.5 mmol) at 130 °C for 30 min. The catalyst was then filtered and contacted with a 5 mL DMF solution of azide (0.5 mmol) and alkyl halide (0.5 mmol). The reaction tube was also sealed in the case and heated at 130 °C for 30 min, leading to a 29% yield, confirming the preferential adsorption of the alkyne on solid single-atom catalysts.

Taking the clean catalyst and the separated reactants in their equilibrium phase at a temperature of 130 °C (solid sodium azide and gas-phase acetylene) as a reference state, one can see from Figure 6b that the first step, namely, the activation of acetylene, is endoergonic. However, the related thermodynamic barrier strongly depends on the coordination of the Cu SAC, and it is minimal (+0.09 eV) in the case of Cu(ads)/C_3N_4, and more significant for Cu species tightly bound to the support: +0.48 eV for Cu(sub)/C_3N_4 and +0.66 eV for Cu(ads)/NG. A more remarkable activation of the C_2H_2 molecule is achieved in the case of smaller barriers, as can be evidenced by inspecting two main structural descriptors of acetylene: the C−C bond distance and the H−C−C bond angle for the molecule in the gas phase are 1.21 Å and 180°. On Cu(ads)/C_3N_4, the C−C bond is elongated up to 1.24 Å, and the bond angle reduces to 161°. On Cu(sub)/C_3N_4, the activation of the acetylene molecule is less pronounced (1.22 Å and 178°), and almost negligible on Cu(ads)/NG (1.21 Å and 179°). For comparison, the acetylene activation has been simulated with the same computational setup over two simple molecules mimicking the Cu(I) and Cu(II) complexes often used as homogeneous catalysts, namely, CuCl and $CuCl_2$ (Table S2 and Figure S8). It results in that C_2H_2 is strongly activated on both substrates, with a slightly more pronounced distortion on CuCl (C−C bond elongation to 1.243 Å and H−C−C bending to 164°) compared to $CuCl_2$ (1.235 Å and 169°). Overall, it can be stated that (i) (Cu)ads/C_3N_4 displays an activity comparable to molecular species adopted as homogeneous catalysts toward C_2H_2 activation and (ii) the coordination of the copper species seems to be the determining factor for its activity, rather than its oxidation state. Thus, a clear trend can be observed, where SAC species displaying more loose coordination to the substrate, such as Cu(ads)/C_3N_4, exhibit higher activity toward acetylene. On the other hand, if the SAC shows three (Cu(sub)/C_3N_4) or even four (Cu(ads)/NG) bonds shorter than 2 Å with N atoms from the substrate, this translates into smaller activity. However, it must be considered that all of the examined SACs are, up to a variable extent, catalytically active: if acetylene is adsorbed on a Cu-free C_3N_4 substrate, then only weak physisorption is reported with no appreciable activation, and no reaction takes place upon coadsorption of sodium azide. As a further test of the proposed mechanism, the adsorption of the reactants in the reversed order has been simulated on Cu(ads)/C_3N_4, the catalyst showing the highest activation of C_2H_2. It resulted in that sodium azide binds strongly to the SAC (−0.96 eV), but the resulting activated complex is unable to bind and react with acetylene, in line with the catalytic experimental evidence. The fact that the reaction proceeds with comparable yield on the three-component reactor (43%) and by dosage of sodium azide on the pre-adsorbed C_2H_2/Cu-SACs (29%) may be ascribed to dynamical processes, allowing the azide species adsorbed on Cu sites to diffuse on the surface, letting the active site free for acetylene activation.

Once the thermodynamic barrier corresponding to the acetylene activation is overcome, the reaction proceeds downhill on all substrates toward the formation of a linear intermediate upon attack of the sodium azide on a C atom from acetylene. The stability of the linear intermediate spans from −1.10 eV with respect to the reactants and the clean substrate for Cu(ads)/NG to −2.73 eV for Cu(sub)/C_3N_4 and −4.19 eV for Cu(ads)/C_3N_4. The cycle is then closed exergonically, with the formation of a pentacyclic triazolate ion coordinated on the Cu SAC, with relative free energies of −3.79 eV for Cu(ads)/NG, −5.34 eV for Cu(sub)/C_3N_4, and −5.47 eV Cu(ads)/C_3N_4. The final step is uphill and leads to the desorption of a sodium triazolate molecule and the regeneration of the clean catalyst. The final barrier to be overcome is larger for Cu(ads)/C_3N_4 (2.27 eV) than Cu(sub)/C_3N_4 (2.14 eV) and Cu(ads)/NG (0.59 eV). The catalyst, thus, can easily activate the reactants, but bind very strongly the products, making their release and the regeneration of the catalyst less favorable. In general, a desorption barrier calculated in this way is just a theoretical construct necessary to close the cycle. Since the experiments are carried out in solution, the solvation of the sodium triazolate will stabilize the reaction product, facilitating the desorption from the catalyst, for instance. Moreover, as explained above, in the experiments, the catalyst is regenerated through washing with ethyl acetate, a procedure that cannot be modeled theoretically.

4. CONCLUSIONS

We have reported a stable single-atom catalyst made of only earth-abundant elements for click chemistry. Compared to literature precedents,[42] this material exploits the textural and electronic properties of mesoporous graphitic carbon nitride to entrap copper species. This mimics the beneficial functions of the homogeneous ligand in a metal complex and surpasses the performance of different state-of-the-art catalysts without evidencing metal leaching or aggregation after the reaction. The enhanced performance could be explained at the molecular level, showing that the reaction proceeds through a barrier given by the activation of the acetylenic moiety on Cu_1. This step is affected mainly by the coordination between the metal and the support. These findings provide further evidence on the importance of optimizing a single-atom catalyst by understanding the exact metal coordination and can help optimize earth-abundant single-atom catalysts for click chemistry and other challenging chemical reactions for the manufacture of fine chemicals and pharmaceuticals.

■ ASSOCIATED CONTENT

Supporting Information

The Supporting Information is available free of charge at https://pubs.acs.org/doi/10.1021/acscatal.1c05610.

Additional characterization and catalytic results of the materials; projected density of state and additional DFT calculation; and NMR characterizations of the reaction products (PDF)

https://doi.org/10.1021/acscatal.1c05610
ACS Catal. 2022, 12, 2947−2958

AUTHOR INFORMATION

Corresponding Author

Gianvito Vilé − *Department of Chemistry, Materials, and Chemical Engineering "Giulio Natta", Politecnico di Milano, 20133 Milano, Italy;* orcid.org/0000-0003-0641-8590; Email: gianvito.vile@polimi.it

Authors

Giovanni Di Liberto − *Department of Materials Science, University of Milano-Bicocca, 20125 Milano, Italy;* orcid.org/0000-0003-4289-2732

Sergio Tosoni − *Department of Materials Science, University of Milano-Bicocca, 20125 Milano, Italy;* orcid.org/0000-0001-5700-4086

Alessandra Sivo − *Department of Chemistry, Materials, and Chemical Engineering "Giulio Natta", Politecnico di Milano, 20133 Milano, Italy*

Vincenzo Ruta − *Department of Chemistry, Materials, and Chemical Engineering "Giulio Natta", Politecnico di Milano, 20133 Milano, Italy*

Maarten Nachtegaal − *Paul Scherrer Institute, 5232 Villigen, Switzerland;* orcid.org/0000-0003-1895-9626

Adam H. Clark − *Paul Scherrer Institute, 5232 Villigen, Switzerland;* orcid.org/0000-0002-5478-9639

Stefano Agnoli − *Department of Chemical Sciences, University of Padova, 35131 Padova, Italy;* orcid.org/0000-0001-5204-5460

Yajun Zou − *Department of Colloid Chemistry, Max Planck Institute of Colloids and Interfaces, Potsdam 14476, Germany*

Aleksandr Savateev − *Department of Colloid Chemistry, Max Planck Institute of Colloids and Interfaces, Potsdam 14476, Germany;* orcid.org/0000-0002-5760-6033

Markus Antonietti − *Department of Colloid Chemistry, Max Planck Institute of Colloids and Interfaces, Potsdam 14476, Germany*

Gianfranco Pacchioni − *Department of Materials Science, University of Milano-Bicocca, 20125 Milano, Italy;* orcid.org/0000-0002-4749-0751

Complete contact information is available at: https://pubs.acs.org/10.1021/acscatal.1c05610

Author Contributions

The manuscript was written through contributions from all authors, and all authors approved the final version of the manuscript.

Notes

The authors declare no competing financial interest.

ACKNOWLEDGMENTS

G.V. thanks Fondazione Bracco and Politecnico di Milano for generous starting up funding. G.D.L., S.T., and G.P. acknowledge the financial support from the Italian Ministry of University and Research (MIUR) through the PRIN Project 20179337R7 and through the grant "Dipartimenti di Eccellenza 2017" entitled "Materials for Energy". Access to the CINECA supercomputing resources was granted via the Italian Super-Computing Resource Allocation (ISCRA). The authors also thank the COST Action 18234 supported by the European Cooperation in Science and Technology (COST), and the Italian Rectors' Conference (CRUI) for supporting publication of this work in open access mode.

REFERENCES

(1) Rostovtsev, V. V.; Green, L. G.; Fokin, V. V.; Sharpless, K. B. A Stepwise Huisgen Cycloaddition Process: Copper(I)-Catalyzed Regioselective 'Ligation' of Azides and Terminal Alkynes. *Angew. Chem., Int. Ed.* **2002**, *41*, 2596−2599.

(2) Cañeque, T.; Müller, S.; Rodriguez, R. Visualizing Biologically Active Small Molecules in Cells Using Click Chemistry. *Nat. Rev. Chem.* **2018**, *2*, 202−215.

(3) Agrahari, A. K.; Bose, P.; Jaiswal, M. K.; Rajkhowa, S.; Singh, A. S.; Hotha, S.; Mishra, N.; Tiwari, V. K. Cu(I)-Catalyzed Click Chemistry in Glycoscience and Their Diverse Applications. *Chem. Rev.* **2021**, *121*, 7638−7956.

(4) Döhler, D.; Michael, P.; Binder, W. H. CuAAC-Based Click Chemistry in Self-Healing Polymers. *Acc. Chem. Res.* **2017**, *50*, 2610−2620.

(5) Bräse, S.; Gil, C.; Knepper, K.; Zimmermann, V. Organic Azides: An Exploding Diversity of a Unique Class of Compounds. *Angew. Chem., Int. Ed.* **2005**, *44*, 5188−5240.

(6) Kulow, R. W.; Wu, J. W.; Kim, C.; Michaudel, Q. Synthesis of Unsymmetrical Sulfamides and Polysulfamides *via* $SuFE_x$ Click Chemistry. *Chem. Sci.* **2020**, *11*, 7807−7812.

(7) Sebest, F.; Dunsford, J. J.; Adams, M.; Pivot, J.; Newman, P. D.; Díez-González, S. Ring-Expanded N-Heterocyclic Carbenes for Copper-Mediated Azide-Alkyne Click Cycloaddition Reactions. *ChemCatChem* **2018**, *10*, 2041−2045.

(8) Zhang, P.; Yamamoto, T.; Suginome, M. Helical Poly(quinoxaline-2,3-diyl)s Bearing 1,2,3-Triazole Pendants: Synthesis by CuAAC and Use as Reusable Abnormal NHC Ligands in Gold Catalysis. *ChemCatChem* **2019**, *11*, 424−429.

(9) Navarro, Y.; García López, J.; Iglesias, M. J.; López Ortiz, F. Chelation-Assisted Interrupted Copper(I)-Catalyzed Azide-Azide-alkyne Domino Reactions: Synthesis of Fully Substituted 5-Triazenyl-1,2,3-triazoles. *Org. Lett.* **2021**, *23*, 334−339.

(10) Liu, E.-C.; Topczewski, J. J. Enantioselective Copper Catalyzed Azide-alkyne Cycloaddition by Dynamic Kinetic Resolution. *J. Am. Chem. Soc.* **2019**, *141*, 5135−5138.

(11) Yang, C.; Flynn, J. P.; Niu, J. Facile Synthesis of Sequence-Regulated Synthetic Polymers Using Orthogonal SuFEx and CuAAC Click Reactions. *Angew. Chem., Int. Ed.* **2018**, *57*, 16194.

(12) Xia, Y.; Campbell, C. T.; Roldan Cuenya, B.; Mavrikakis, M. Introduction: Advanced Materials and Methods for Catalysis and Electrocatalysis by Transition Metals. *Chem. Rev.* **2021**, *121*, 563−566.

(13) Wen, J.; Wu, K.; Yang, D.; Tian, J.; Huang, Z.; Filatov, A. S.; Lei, A.; Lin, X.-M. Low-Pressure Flow Chemistry of CuAAC Click Reaction Catalyzed by Nanoporous Aucu Membrane. *ACS Appl. Mater. Interfaces* **2018**, *10*, 25930−25935.

(14) Vilé, G.; Liu, J.; Zhang, Z. Surface Engineering of a Cu-Based Heterogeneous Catalyst for Efficient Azide-Alkyne Click Cycloaddition. *React. Chem. Eng.* **2021**, *6*, 1878−1883.

(15) Roy, S.; Chatterjee, T.; Pramanik, M.; Singha Roy, A.; Bhaumik, A.; Islam, S. M. Cu(II)-Anchored Functionalized Mesoporous SBA-15: An Efficient and Recyclable Catalyst for the One-Pot Click Reaction in Water. *J. Mol. Catal. A* **2014**, *386*, 78.

(16) Elavarasan, S.; Bhaumik, A.; Sasidharan, M. An Efficient Mesoporous Cu-Organic Nanorod for Friedländer Synthesis of Quinoline and Click Reactions. *ChemCatChem* **2019**, *11*, 4340.

(17) Xia, Y.; Campbell, C. T.; Roldan Cuenya, B.; Mavrikakis, M. Advanced Materials and Methods for Catalysis and Electrocatalysis by Transition Metals. *Chem. Rev.* **2021**, *121*, 563−566.

(18) Liu, L.; Corma, A. Metal Catalysts for Heterogeneous Catalysis: From Single Atoms to Nanoclusters and Nanoparticles. *Chem. Rev.* **2018**, *118*, 4981−5079.

(19) Mavrikakis, M.; Bäumer, M.; Freund, H.-J.; Nørskov, J. K. Structure Sensitivity of CO Dissociation on Rh surfaces. *Catal. Lett.* **2002**, *81*, 153−156.

(20) Vogt, C.; Groeneveld, E.; Kamsma, G.; Nachtegaal, M.; Lu, L.; Kiely, C. J.; Berben, P. H.; Meirer, F.; Weckhuysen, B. M. Unravelling Structure Sensitivity in CO_2 Hydrogenation Over Nickel. *Nat. Catal.* **2018**, *1*, 127−134.

(21) Hartman, T.; Geitenbeek, R. G.; Wondergem, C. S.; van der Stam, W.; Weckhuysen, B. M. Operando Nanoscale Sensors in Catalysis: All Eyes on Catalyst Particles. *ACS Nano* **2020**, *14*, 3725−3735.
(22) Wang, A.; Li, J.; Zhang, T. Heterogeneous Single-Atom Catalysis. *Nat. Rev. Chem.* **2018**, *2*, 65−81.
(23) Hackett, S. F. J.; Brydson, R. M.; Gass, M. H.; Harvey, I.; Newman, A. D.; Wilson, K.; Lee, A. F. High-Activity, Single-Site Mesoporous Pd/Al_2O_3 Catalysts for Selective Aerobic Oxidation of Allylic Alcohols. *Angew. Chem., Int. Ed.* **2007**, *46*, 8593−8596.
(24) Peterson, E. J.; DeLaRiva, A. T.; Lin, S.; Johnson, R. S.; Guo, H.; Miller, J. T.; Kwak, J. H.; Peden, C. H. F.; Kiefer, B.; Allard, L. F.; Ribeiro, F. H.; Datye, A. K. Low-Temperature Carbon Monoxide Oxidation Catalysed by Regenerable Atomically Dispersed Palladium on Alumina. *Nat. Commun.* **2014**, *5*, No. 4885.
(25) Li, M.; Duanmu, K.; Wan, C.; Cheng, T.; Zhang, L.; Dai, S.; Chen, W.; Zhao, Z.; Li, P.; Fei, H.; Zhu, Y.; Yu, R.; Luo, J.; Zang, K.; Lin, Z.; Ding, M.; Huang, J.; Sun, H.; Guo, J.; Pan, X.; Goddard, W. A.; Sautet, P.; Huang, Y.; Duan, X. Single-Atom Tailoring of Platinum Nanocatalysts for High-Performance Multifunctional Electrocatalysis. *Nat. Catal.* **2019**, *2*, 495−503.
(26) Yin, X.-P.; Wang, H.-J.; Tang, S.-F.; Lu, X.-L.; Shu, M.; Si, R.; Lu, T.-B. Engineering the Coordination Environment of Single-Atom Platinum Anchored on Graphdiyne for Optimizing Electrocatalytic Hydrogen Evolution. *Angew. Chem., Int. Ed.* **2018**, *57*, 9382−9386.
(27) He, T.; Puente Santiago, A. R.; Du, A. Atomically Embedded Asymmetrical Dual-Metal Dimers on N-Doped Graphene for Ultra-Efficient Nitrogen Reduction Reaction. *J. Catal.* **2020**, *388*, 77−83.
(28) Zhao, C.; Wang, Y.; Li, Z.; Chen, W.; Xu, Q.; He, D.; Xi, D.; Zhang, Q.; Yuan, T.; Qu, Y.; Yang, J.; Zhou, F.; Yang, Z.; Wang, X.; Wang, J.; Luo, J.; Li, Y.; Duan, H.; Wu, Y.; Li, Y. Solid-Diffusion Synthesis of Single-Atom Catalysts Directly from Bulk Metal for Efficient CO_2 Reduction. *Joule* **2019**, *3*, 584−594.
(29) Zang, W.; Sumboja, A.; Ma, Y.; Zhang, H.; Wu, Y.; Wu, S.; Wu, H.; Liu, Z.; Guan, C.; Wang, J.; Pennycook, S. J. Single Co Atoms Anchored in Porous N-Doped Carbon for Efficient Zinc-Air Battery Cathodes. *ACS Catal.* **2018**, *8*, 8961−8969.
(30) Yan, H.; Zhao, X.; Guo, N.; Lyu, Z.; Du, Y.; Xi, S.; Guo, R.; Chen, C.; Chen, Z.; Liu, W.; Yao, C.; Li, J.; Pennycook, S. J.; Chen, W.; Su, C.; Zhang, C.; Lu, J. Atomic Engineering of High-Density Isolated Co Atoms on Graphene with Proximal-Atom Controlled Reaction Selectivity. *Nat. Commun.* **2018**, *9*, No. 3197.
(31) Deng, J.; Li, H.; Xiao, J.; Tu, Y.; Deng, D.; Yang, H.; Tian, H.; Li, J.; Ren, P.; Bao, X. Triggering the Electrocatalytic Hydrogen Evolution Activity of the Inert Two-Dimensional MoS_2 Surface *via* Single-Atom Metal Doping. *Energy Environ. Sci.* **2015**, *8*, 1594−1601.
(32) Yang, S.; Kim, J.; Tak, Y. J.; Soon, A.; Lee, H. Single-Atom Catalyst of Platinum Supported on Titanium Nitride for Selective Electrochemical Reactions. *Angew. Chem., Int. Ed.* **2016**, *55*, 2058−2062.
(33) Zhao, Y.; Zhou, H.; Chen, W.; Tong, Y.; Zhao, C.; Lin, Y.; Jiang, Z.; Zhang, Q.; Xue, Z.; Cheong, W.-C.; Jin, B.; Zhou, F.; Wang, W.; Chen, M.; Hong, X.; Dong, J.; Wei, S.; Li, Y.; Wu, Y. Two-Step Carbothermal Welding to Access Atomically Dispersed Pd_1 on Three-Dimensional Zirconia Nanonet for Direct Indole Synthesis. *J. Am. Chem. Soc.* **2019**, *141*, 10590−10594.
(34) Gawande, M. B.; Fornasiero, P.; Zboril, R. Carbon-Based Single-Atom Catalysts for Advanced Applications. *ACS Catal.* **2020**, *10*, 2231−2259.
(35) Hulva, J.; Meier, M.; Bliem, R.; Jakub, Z.; Kraushofer, F.; Schmid, M.; Diebold, U.; Franchini, C.; Parkinson, G. S. Unraveling CO Adsorption on Model Single-Atom Catalysts. *Science* **2021**, *371*, 375−379.
(36) Daelman, N.; Capdevila-Cortada, M.; López, N. Dynamic Charge and Oxidation State of Pt/CeO_2 Single-Atom Catalysts. *Nat. Mater.* **2019**, *18*, 1215−1221.
(37) Thang, H. V.; Pacchioni, G. On the Real Nature of Rh Single Atom Catalysts Dispersed on the ZrO_2 Surface. *ChemCatChem* **2020**, *12*, 2595−2604.
(38) Resasco, J.; DeRita, L.; Dai, S.; Chada, J. P.; Xu, M.; Yan, X.; Finzel, J.; Hanukovich, S.; Hoffman, A. S.; Graham, G. W.; Bare, S. R.; Pan, X.; Christopher, P. Uniformity is Key in Defining Structure-Function Relationships for Atomically Dispersed Metal Catalysts: the case of Pt/CeO_2. *J. Am. Chem. Soc.* **2020**, *142*, 169−184.
(39) Vilé, G.; Albani, D.; Nachtegaal, M.; Chen, Z.; Dontsova, D.; Antonietti, M.; López, N.; Pérez-Ramírez, J. A Stable Single-Site Palladium Catalyst for Hydrogenations. *Angew. Chem., Int. Ed.* **2015**, *54*, 11265−11269.
(40) Liu, J.; Zou, Y.; Cruz, D.; Savateev, A.; Antonietti, M.; Vilé, G. Ligand-Metal Charge Transfer Induced *via* Adjustment of Textural Properties Controls the Performance of Single-Atom Catalysts During Photocatalytic Degradation. *ACS Appl. Mater. Interfaces* **2021**, *13*, 25858−25867.
(41) Vilé, G.; Sharma, P.; Nachtegaal, M.; Tollini, F.; Moscatelli, D.; Sroka-Bartnicka, A.; Tomanec, O.; Petr, M.; Filip, J.; Pieta, I. S.; Zbořil, R.; Gawande, M. B. An Earth-Abundant Ni-Based Single-Atom Catalyst for Selective Photodegradation of Pollutants. *Solar RRL* **2021**, *5*, No. 2100176.
(42) Ren, P.; Li, Q.; Song, T.; Wang, Z.; Motokura, K.; Yang, Y. Highly Efficient and Stable Atomically Dispersed Cu Catalyst for Azide-Alkyne Cycloaddition Reaction. *ChemCatChem* **2021**, *13*, 3960−3966.
(43) Clark, A. H.; Imbao, J.; Frahmb, R.; Nachtegaalal, M. ProQEXAFS: a Highly Optimized Parallelized Rapid Processing Software for QEXAFS Data. *J. Synchrotron Rad.* **2020**, *27*, 551−557.
(44) Ravel, B.; Newville, M. ATHENA, ARTEMIS, HEPHAESTUS: Data Analysis for X-ray Absorption Spectroscopy Using IFEFFIT. *J. Synchrotron Rad.* **2005**, *12*, 537−541.
(45) Kresse, G.; Hafner, J. Ab Initio Molecular Dynamics for Liquid Metals. *Phys. Rev. B* **1993**, *47*, 558−561.
(46) Kresse, G.; Furthmüller, J. Efficiency of Ab-Initio Total Energy Calculations for Metals. *Comput. Mater. Sci.* **1996**, *6*, 15−50.
(47) Blöchl, P. E. Projector augmented-wave method. *Phys. Rev. B* **1994**, *50*, 17953−17979.
(48) Kresse, G.; Joubert, D. From Ultrasoft Pseudopotentials to the Projector Augmented-Wave Method. *Phys. Rev. B* **1999**, *59*, 1758−1775.
(49) Perdew, J. P.; Burke, K.; Ernzerhof, M. Generalized Gradient Approximation Made Simple. *Phys. Rev. Lett.* **1996**, *77*, 3865−3868.
(50) Grimme, S.; Antony, J.; Ehrlich, S.; Krieg, H. A Consistent and Accurate Ab Initio Parametrization of Density Functional Dispersion Correction (DFT-D) for the 94 Elements H-Pu. *J. Chem. Phys.* **2010**, *132*, No. 154104.
(51) Grimme, S.; Ehrlich, S.; Goerigk, L. Effect of the Damping Function in Dispersion Corrected Density Functional Theory. *J. Comput. Chem.* **2011**, *32*, 1456−1465.
(52) Bardelang, D.; Camerel, F.; Ziessel, R.; Schmutzc, M.; Hannon, M. J. New Organogelators Based on Cyclotriveratrylene Platforms Bearing 2-Dimethylacetal-5-Carbonylpyridine Fragments. *J. Mater. Chem.* **2008**, *18*, 489.
(53) Wang, Y.; Wang, X.; Antonietti, M. Polymeric Graphitic Carbon Nitride as a Heterogeneous Organocatalyst: From Photochemistry to Multipurpose Catalysis to Sustainable Chemistry. *Angew. Chem., Int. Ed.* **2012**, *51*, 68−89.
(54) Di Liberto, G.; Tosoni, S.; Pacchioni, G. *Catal. Sci. Technol.* **2021**, *11*, 3589−3598.
(55) Nørskov, J. K.; Bligaard, T.; Logadottir, A.; Kitchin, J. R.; Chen, J. G.; Pandelov, S.; Stimming, U. Trends in the Exchange Current for Hydrogen Evolution. *J. Electrochem. Soc.* **2005**, *152*, J23.
(56) Nørskov, J. K.; Rossmeisl, J.; Logadottir, A.; Lindqvist, L.; Kitchin, J. R.; Bligaard, T.; Jónsson, H. Origin of the Overpotential for Oxygen Reduction at a Fuel-Cell Cathode. *J. Phys. Chem. B* **2004**, *108*, 17886−17892.
(57) Chan, K.; Tsai, C.; Hansen, H. A.; Nørskov, J. K. Molybdenum Sulfides and Selenides as Possible Electrocatalysts for CO_2 Reduction. *ChemCatChem* **2014**, *6*, 1899−1905.
(58) Calle-Vallejo, F.; Pohl, M. D.; Reinisch, D.; Loffreda, D.; Sautet, P.; Bandarenk, A. S. Why Conclusions from Platinum Model Surfaces

https://doi.org/10.1021/acscatal.1c05610
ACS Catal. 2022, 12, 2947−2958

Do Not Necessarily Lead to Enhanced Nanoparticle Catalysts for the Oxygen Reduction Reaction. *Chem. Sci.* **2017**, *8*, 2283−2289.
(59) Shang, R.; Steinmann, S. N.; Xu, B.-Q.; Sautet, P. Mononuclear Fe in N-Doped Carbon: Computational Elucidation of Active Sites for Electrochemical Oxygen Reduction and Oxygen Evolution Reactions. *Catal. Sci. Technol.* **2020**, *10*, 1006−1014.
(60) Van Dao, D.; Cipriano, L. A.; Di Liberto, G.; Nguyen, T. T. D.; Ki, S.-W.; Son, H.; Kim, G.-C.; Lee, K. H.; Yang, J.-K.; Yu, Y.-T.; Pacchioni, G.; Lee, I.-H. Plasmonic Au Nanoclusters Dispersed in Nitrogen-Doped Graphene as a Robust Photocatalyst for Light-to-Hydrogen Conversion. *J. Mater. Chem. A* **2021**, *9*, 22810.
(61) Cox, J.; Wagman, D. D.; Medvedev, V. A. *CODATA: Key-Values for Thermodynamics*; Hemisphere Publishing Corp.: New York, 1989.
(62) Kleymenov, E.; van Bokhoven, J. A.; David, C.; Glatzel, P.; Janousch, M.; Alonso-Mori, R.; Studer, M.; Willimann, M.; Bergamaschi, A.; Henrich, B.; Nachtegaal, M. Five-Element Johann-Type X-Ray Emission Spectrometer with a Single-Photon-Counting Pixel Detector. *Rev. Sci. Instrum.* **2011**, *82*, No. 065107.
(63) Groenewolt, M.; Antonietti, M. Synthesis of gC_3N_4 Nanoparticles in Mesoporous Silica Host Matrices. *Adv. Mater.* **2005**, *17*, 1789−1792.
(64) Chen, Z.; Pronkin, S.; Fellinger, T.-P.; Kailasam, K.; Vilé, G.; Albani, D.; Krumeich, F.; Leary, R.; Barnard, J.; Thomas, J. M.; Pérez-Ramírez, J.; Antonietti, M.; Dontsova, D. Merging Single-Atom-Dispersed Silver and Carbon Nitride to a Joint Electronic System via Copolymerization with Silver Tricyanomethanide. *ACS Nano* **2016**, *10*, 3166−3175.
(65) Zhang, J.-R.; Ma, Y.; Wang, S.-Y.; Ding, J.; Gao, B.; Kan, E.; Hua, W. Accurate K-edge X-ray Photoelectron and Absorption Spectra of g-C_3N_4 Nanosheets by First-Principles Simulations and Reinterpretations. *Phys. Chem. Chem. Phys.* **2019**, *21*, 22819−22830.
(66) Biesinger, M. C. Advanced Analysis of Copper X-ray Photoelectron Spectra. *Surf. Interface Anal.* **2017**, *49*, 1325−1334.
(67) Cometto, C.; Ugolotti, A.; Grazietti, E.; Moretto, A.; Bottaro, G.; Armelao, L.; Di Valentin, C.; Calvillo, L.; Granozzi, G. Copper Single-Atoms Embedded in 2D Graphitic Carbon Nitride for the CO_2 Reduction. *npj 2D Mater. Appl.* **2021**, *5*, No. 63.
(68) Moretti, G.; Palma, A.; Paparazzo, E.; Satta, M. Auger Parameter and Wagner Plot Studies of Small Copper Clusters. *Surf. Sci.* **2016**, *646*, 298−305.
(69) Tomson, N. C.; Williams, K. D.; Dai, X.; Sproules, S.; DeBeer, S.; Warren, T. H.; Wieghardt, K. Re-Evaluating the Cu K Pre-Edge XAS Transition in Complexes with Covalent Metal-Ligand Interactions. *Chem. Sci.* **2015**, *6*, 2474−2487.
(70) Chen, Z.; Zhao, J.; Cabrera, C. R.; Chen, Z. Computational Screening of Efficient Single-Atom Catalysts Based on Graphitic Carbon Nitride (g-C_3N_4) for Nitrogen Electroreduction. *Small Methods* **2019**, *3*, No. 1800368.
(71) Biondi, C.; Bonamico, M.; Torelli, L.; Vaciago, A. On the structure and water content of copper(II) tricyanomethanide. *Chem. Commun.* **1965**, 191−192.

https://doi.org/10.1021/acscatal.1c05610
ACS Catal. 2022, 12, 2947−2958